

Ultrasonic scalpel based on fusiform phononic crystal structure

Sha Wang(王莎), Junjie Shan(单俊杰), and Shuyu Lin(林书玉)

Citation: Chin. Phys. B, 2024, 33 (**10**): 104302. DOI: 10.1088/1674-1056/ad6a0c
Journal homepage: http://cpb.iphy.ac.cn; http://iopscience.iop.org/cpb

What follows is a list of articles you may be interested in

Inverse design of nonlinear phononic crystal configurations based on multi-label classification learning neural networks

Kunqi Huang(黄坤琦), Yiran Lin(林懿然), Yun Lai(赖耘), and Xiaozhou Liu(刘晓宙)
Chin. Phys. B, 2024, 33 (**10**): 104301. DOI: 10.1088/1674-1056/ad6b85

Sensing the heavy water concentration in an H_2O—D_2O mixture by solid—solid phononic crystals

Mohammadreza Rahimi and Ali Bahrami
Chin. Phys. B, 2024, 33 (**4**): 044301. DOI: 10.1088/1674-1056/ad0bf5

Nonlinear wave propagation in acoustic metamaterials with bilinear nonlinearity

Shiqi Liang(梁诗琪), Jiehui Liu(刘杰惠), Yun Lai(赖耘), and Xiaozhou Liu(刘晓宙)
Chin. Phys. B, 2023, 32 (**4**): 044301. DOI: 10.1088/1674-1056/ac9783

Tunable topological interface states and resonance states of surface waves based on the shape memory alloy

Shao-Yong Huo(霍绍勇), Long-Chao Yao(姚龙超), Kuan-Hong Hsieh(谢冠宏), Chun-Ming Fu(符纯明), Shih-Chia Chiu(邱士嘉), Xiao-Chao Gong(龚小超), and Jian Deng(邓健)
Chin. Phys. B, 2023, 32 (**3**): 034303. DOI: 10.1088/1674-1056/ac8727

Analysis on vibration characteristics of large-size rectangular piezoelectric composite plate based on quasi-periodic phononic crystal structure

Li-Qing Hu(胡理情), Sha Wang(王莎), and Shu-Yu Lin(林书玉)
Chin. Phys. B, 2022, 31 (**5**): 054302. DOI: 10.1088/1674-1056/ac3649

Ultrasonic scalpel based on fusiform phononic crystal structure

Sha Wang(王莎)[1,2], Junjie Shan(单俊杰)[3,†], and Shuyu Lin(林书玉)[2,‡]

[1] *Ocean College, Jiangsu University of Science and Technology, Zhenjiang* 212100, *China*
[2] *Shaanxi Key Laboratory of Ultrasonics, School of Physics and Information Technology, Shaanxi Normal University, Xi'an* 710119, *China*
[3] *National Laboratory of Solid State Microstructures, School of Physics, Collaborative Innovation Center of Advanced Microstructures, Nanjing University, Nanjing* 210093, *China*

(Received 1 June 2024; revised manuscript received 17 July 2024; accepted manuscript online 1 August 2024)

In response to the ultrasonic scalpels with the vibrational modal coupling which leads to a decrease in efficiency, an ultrasonic scalpel based on fusiform phononic crystals (PnCs) is proposed. An accurate theoretical model is constructed, which is mainly composed of electromechanical equivalent circuit models to analyze the frequency response function and the frequency response curves of the admittance. Bragg band gaps exist in the fusiform PnCs owing to the periodic constraint, which can suppress the corresponding vibrational modes. The vibration characteristics (vibration mode, frequency, and displacement distribution) of the ultrasonic scalpel are analyzed, and the validity of the electromechanical equivalent circuit method is verified. The results indicate that other vibration modes near the working frequency can be isolated. In addition, blades based on fusiform PnCs have a function akin to that of the horn, which enables displacement amplification.

Keywords: phononic crystals, ultrasonic scalpel, bandgap, vibration characteristics

PACS: 43.40.+s, 43.35.+d, 43.20.+g, 63.20.–e **DOI:** 10.1088/1674-1056/ad6a0c

1. Introduction

Ultrasonic scalpels have demonstrated significant potential in ultrasound medicine, which is widely used in plastic surgery,[1] ophthalmology,[2,3] and neurology.[4,5] Whether cutting soft tissues such as blood vessels and livers or hard tissues such as bone, ultrasonic scalpels have the advantages of safety, less bleeding, flexibility, and low labor requirements.[6–9] The ultrasonic scalpel mainly includes a piezoelectric transducer, a horn, and various blades.[10] Among all elements, the blade is one of the most important, which is specially used to cut or suck different tissues. Because of the complex structures of blades, ultrasonic scalpels have many vibration modes near the working frequency. In the working process of an ultrasonic scalpel, the working frequency is easy to shift due to external interference and load to excite other resonance modes, reducing the working efficiency.[11] Therefore, it is necessary to suppress other vibration modes near the working frequency.

On the other hand, phononic crystals (PnCs) are functional materials with a periodic structure first proposed by Kushwah *et al*. in the study of nickel/aluminum two-dimensional solid periodic composite media.[12] PnCs can prohibit or suppress the propagation of elastic waves in the frequency ranges for the band gap.[13–15] PnCs are widely used in vibration suppression due to the unique vibration characteristics of the band gap.[16–18] Wang *et al*. improved the longitudinal radiating surface displacement distribution by suppressing the radial vibration of a large-size ultrasonic plastic welding system using PnCs.[19] Zhang *et al.* designed several new complex cells to obtain a lower frequency band gap or widen the low-frequency band gap for vibration control of piping systems.[20] Ruan *et al*. designed a single-phase spiral-shaped PnCs based on the vibration frequency spectrums in "ChangJing 9" to protect electronic equipment and precision instruments on the ship.[21]

In general, PnCs are constructed by the periodic arrangement of two materials.[22,23] However, if the blade is made of two materials in a periodic structure, it will lead to problems such as stress concentration and excessive sound reflection. Therefore, the blade must be made of one material, which is a challenge for applying PnCs in the ultrasonic scalpel.

Here, the blades of ultrasonic scalpel based on fusiform PnCs are proposed. The unique band gap properties of PnCs are used to suppress other modes near the working frequency of the ultrasonic scalpel. A theoretical model is developed to analyze the vibration characteristics of the ultrasonic scalpel and the frequency response function of the blades, which can provide effective guidance for the design of ultrasonic scalpels. It is expected that PnC structures may provide a new perspective for the analysis and design of ultrasonic scalpels.

2. Structure and principle

2.1. Structure of blades

The ultrasonic scalpel is composed of a transducer, a horn, and a blade, as shown in Fig. 1. In order to facilitate the subsequent theoretical analysis, the ultrasonic scalpel is

†Corresponding author. E-mail: junjieshan@nju.edu.cn
‡Corresponding author. E-mail: sylin@snnu.edu.cn

© 2024 Chinese Physical Society and IOP Publishing Ltd

divided into the parts of D, E, P, F, G, H, I, J, K, L, M, and N.

When the blade vibrates at ultrasonic frequencies, the tissue will rupture, and the heat generated by the vibration can lead to protein condensation in the process of tissue–tool interaction, which can realize simultaneous cutting and sealing. However, because of the complex structure of the ultrasonic scalpel, there are many vibration modes near the working frequency. Excessive vibration modes reduce efficiency, so it is necessary to suppress unnecessary modes near the working frequency. The blade as the main vibration transmission device of the ultrasonic scalpel is the key to suppression for vibration modes near the working frequency.

Ultrasonic scalpels usually operate at ultrasonic frequency and with high amplitude. Therefore, there are requirements for the strength of the blade, which must be made of one material. To satisfy the demand of an ultrasonic scalpel, a blade with fusiform PnCs is designed which is different from PnCs with two materials, as shown in Fig. 2. Due to the variation of the cross-sectional radius, a Bragg band gap will be formed by the periodic constraint when the acoustic wave propagates in it. a is the lattice constant. a_1 and a_2 are the lengths of A and B. d_1 and d_2 are the diameters. In order to compare the differences between the ultrasonic scalpel based on the PnCs structure and the conventional ultrasonic scalpel, the conventional blade is also designed, as shown in Fig. 1.

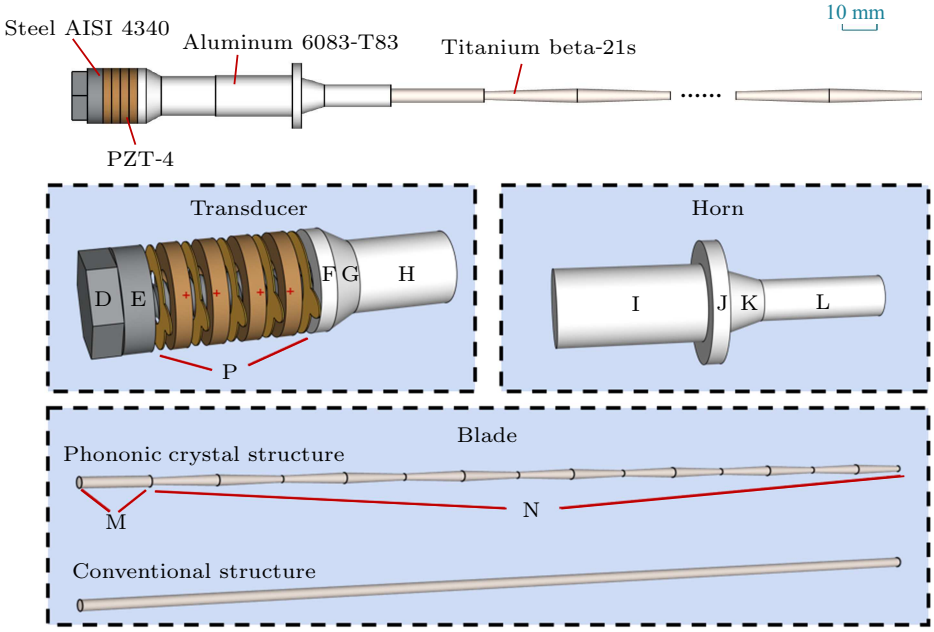


Fig. 1. The schematic diagram of the ultrasonic scalpel.

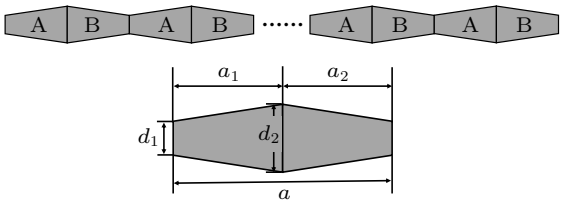


Fig. 2. The schematic diagram for the blade based on the fusiform PnCs.

The propagation of elastic waves can be suppressed within the band gap of PnCs structures. Therefore, it is necessary to analyze the band gap range of the blade and the resonance frequency of the ultrasonic scalpel. Two methods are employed here for analyzing the frequency response function and vibration characteristic: the electromechanical equivalent circuit method and the finite element method (FEM).

2.2. Electromechanical equivalent circuit method

The electromechanical equivalent circuits can be connected in series, parallel, or cascade according to the boundary conditions. Because the force and vibration velocity at the contacting surfaces of the A and B parts are continuous, the electromechanical equivalent circuit of A and B can be cascaded, as shown in Fig. 3.

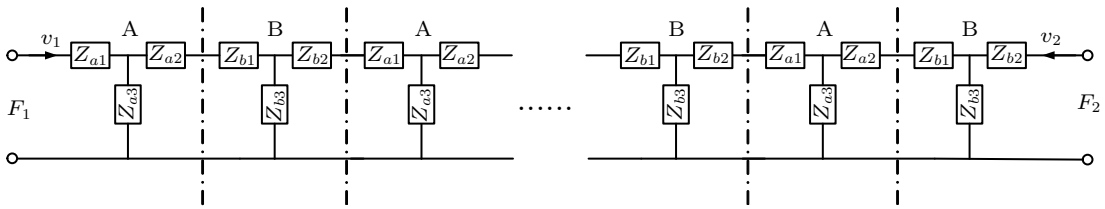


Fig. 3. The electromechanical equivalent circuit method of the blade based on the fusiform PnCs.

The impedance expressions in the figure are related to the area function. Here, the three area functions are discussed, which are the cone, exponent, and catenary. For the cone, Z_{a1}, Z_{a2}, Z_{a3}, Z_{b1}, Z_{b2}, and Z_{b3} can be expressed as

$$\begin{aligned} Z_{a1} &= -\mathrm{j}\frac{\rho c S_1}{k a_1}\left(\sqrt{\frac{S_2}{S_1}}-1\right) \\ &\quad -\mathrm{j}\rho c S_1 \cot(k a_1)+\mathrm{j}\frac{\rho c\sqrt{S_1 S_2}}{\sin(k a_1)}, \end{aligned} \tag{1}$$

$$\begin{aligned} Z_{a2} &= -\mathrm{j}\frac{\rho c S_2}{k a_1}\left(\sqrt{\frac{S_1}{S_2}}-1\right) \\ &\quad -\mathrm{j}\rho c S_2 \cot(k a_1)+\mathrm{j}\frac{\rho c\sqrt{S_1 S_2}}{\sin(k a_1)}, \end{aligned} \tag{2}$$

$$Z_{a3} = \frac{\rho c\sqrt{S_1 S_2}}{\mathrm{j}\sin(k a_1)}, \tag{3}$$

$$\begin{aligned} Z_{b1} &= -\mathrm{j}\frac{\rho c S_2}{k a_2}\left(\sqrt{\frac{S_1}{S_2}}-1\right) \\ &\quad -\mathrm{j}\rho c S_2 \cot(k a_2)+\mathrm{j}\frac{\rho c\sqrt{S_1 S_2}}{\sin(k a_2)}, \end{aligned} \tag{4}$$

$$\begin{aligned} Z_{b2} &= -\mathrm{j}\frac{\rho c S_1}{k a_2}\left(\sqrt{\frac{S_2}{S_1}}-1\right) \\ &\quad -\mathrm{j}\rho c S_1 \cot(k a_2)+\mathrm{j}\frac{\rho c\sqrt{S_1 S_2}}{\sin(k a_2)}, \end{aligned} \tag{5}$$

$$Z_{b3} = \frac{\rho c\sqrt{S_1 S_2}}{\mathrm{j}\sin(k a_2)}, \tag{6}$$

where ρ is the bulk density of the material, j is imaginary unit, k is the wave number, $k=\omega/c$, ω is the angular frequency, $c=\sqrt{E/\rho}$, E is Young's modulus, $S_1=\pi d_1^2/4$, $S_2=\pi d_2^2/4$. For the exponent, Z_{a1}, Z_{a2}, Z_{a3}, Z_{b1}, Z_{b2}, and Z_{b3} can be expressed as

$$\begin{aligned} Z_{a1} &= \mathrm{j}\frac{\rho c S_1 \beta_a}{k}-\mathrm{j}\rho c S_1\frac{k_i'}{k}\cot\left(k_i' a_1\right) \\ &\quad +\mathrm{j}\frac{k_i'\rho c\sqrt{S_1 S_2}}{k\sin\left(k_i' a_1\right)}, \end{aligned} \tag{7}$$

$$\begin{aligned} Z_{a2} &= -\mathrm{j}\frac{\rho c S_2 \beta_a}{k}-\mathrm{j}\rho c S_2\frac{k_i'}{k}\cot\left(k_i' a_1\right) \\ &\quad +\mathrm{j}\frac{k_i'\rho c\sqrt{S_1 S_2}}{k\sin\left(k_i' a_1\right)}, \end{aligned} \tag{8}$$

$$Z_{a3} = \frac{k_i'\rho c\sqrt{S_1 S_2}}{\mathrm{j}k\sin\left(k_i' a_1\right)}, \tag{9}$$

$$\begin{aligned} Z_{b1} &= \mathrm{j}\frac{\rho c S_2 \beta_b}{k}-\mathrm{j}\rho c S_2\frac{k_i'}{k}\cot\left(k_i' a_2\right) \\ &\quad +\mathrm{j}\frac{k_i'\rho c\sqrt{S_1 S_2}}{k\sin\left(k_i' a_2\right)}, \end{aligned} \tag{10}$$

$$\begin{aligned} Z_{b2} &= -\mathrm{j}\frac{\rho c S_1 \beta_b}{k}-\mathrm{j}\rho c S_1\frac{k_i'}{k}\cot\left(k_i' a_2\right) \\ &\quad +\mathrm{j}\frac{k_i'\rho c\sqrt{S_1 S_2}}{k\sin\left(k_i' a_2\right)}, \end{aligned} \tag{11}$$

$$Z_{b3} = \frac{k_i'\rho c\sqrt{S_1 S_2}}{\mathrm{j}k\sin\left(k_i' a_2\right)}, \tag{12}$$

where $\beta_a=\ln\sqrt{S_1/S_2}/a_1$, $\beta_b=\ln\sqrt{S_2/S_1}/a_2$, $k_i'=\sqrt{k^2-\beta_{a(b)}^2}$. For the catenary, Z_{a1}, Z_{a2}, Z_{a3}, Z_{b1}, Z_{b2}, and Z_{b3} can be expressed as

$$\begin{aligned} Z_{a1} &= -\mathrm{j}\rho c S_1\frac{k_c'}{k}\cot\left(k_c' a_1\right)+\mathrm{j}\frac{k_c'\rho c\sqrt{S_1 S_2}}{k\sin\left(k_c' a_1\right)}, \end{aligned} \tag{13}$$

$$\begin{aligned} Z_{a2} &= \mathrm{j}\frac{\rho c S_1\gamma}{k}\cosh[\gamma a_1]\sinh[\gamma a_1] \\ &\quad -\mathrm{j}\rho c S_2\frac{k_c'}{k}\cot\left(k' a_1\right)+\mathrm{j}\frac{k_c'\rho c\sqrt{S_1 S_2}}{k\sin\left(k_c' a_1\right)}, \end{aligned} \tag{14}$$

$$Z_{a3} = \frac{k_c'\rho c\sqrt{S_1 S_2}}{\mathrm{j}k\sin\left(k_c' a_1\right)}, \tag{15}$$

$$\begin{aligned} Z_{b1} &= \mathrm{j}\frac{\rho c S_2\gamma}{k}\tanh(\gamma a_2) \\ &\quad -\mathrm{j}\rho c S_2\frac{k_c'}{k}\cot\left(k_c' a_2\right)+\mathrm{j}\frac{k_c'\rho c\sqrt{S_1 S_2}}{k\sin\left(k_c' a_2\right)}, \end{aligned} \tag{16}$$

$$\begin{aligned} Z_{a2} &= -\mathrm{j}\rho c S_1\frac{k_c'}{k}\cot\left(k_c' a_2\right)+\mathrm{j}\frac{k_c'\rho c\sqrt{S_1 S_2}}{k\sin\left(k_c' a_2\right)}, \end{aligned} \tag{17}$$

$$Z_{a3} = \frac{k_c'\rho c\sqrt{S_1 S_2}}{\mathrm{j}k\sin\left(k_c' a_2\right)}, \tag{18}$$

where

$$\gamma=\frac{\operatorname{arccosh}\sqrt{S_2/S_1}}{a_{1(2)}},\quad k_c'=\sqrt{k^2-\gamma^2}.$$

The electromechanical equivalent circuit in Fig. 3 can be considered as a cascade of several two-terminal networks, as shown in Fig. 4. According to Fig. 4, the relationship between force and vibration velocity can be expressed as

$$\begin{bmatrix} F_i' \\ v_i' \end{bmatrix} = \begin{bmatrix} A_{a(b)} & B_{a(b)} \\ C_{a(b)} & D_{a(b)} \end{bmatrix} \begin{bmatrix} F_{i+1}' \\ -v_{i+1}' \end{bmatrix}, \tag{19}$$

where $i=1,3,5,\ldots$,

$$\begin{aligned} A_{a(b)} &= \frac{Z_{11a(b)}}{Z_{21a(b)}},\quad B_{a(b)}=\frac{\Delta Z_{a(b)}}{Z_{21}}, \\ C_{a(b)} &= \frac{1}{Z_{21a(b)}},\quad D_{a(b)}=\frac{Z_{22a(b)}}{Z_{21a(b)}}, \\ Z_{11a(b)} &= Z_{a(b)1}+Z_{a(b)3}, \\ Z_{22a(b)} &= Z_{a(b)2}+Z_{a(b)3}, \\ Z_{12a(b)} &= Z_{21a(b)}=Z_{a(b)3}, \\ \Delta Z_{a(b)} &= \begin{vmatrix} Z_{11a(b)} & Z_{12a(b)} \\ Z_{21a(b)} & Z_{22a(b)} \end{vmatrix}. \end{aligned}$$

The parameters of the two-terminal network are related as follows:

$$T=\begin{bmatrix} A & B \\ C & D \end{bmatrix}=T_a T_b T_a\cdots T_b T_a T_b, \tag{20}$$

where $T_{a(b)}=\begin{bmatrix} A_{a(b)} & B_{a(b)} \\ C_{a(b)} & D_{a(b)} \end{bmatrix}$.

Thus, the vibration velocity ratio can be obtained as

$$\frac{v_1}{v_2}=\frac{I_1}{I_2}=-D. \tag{21}$$

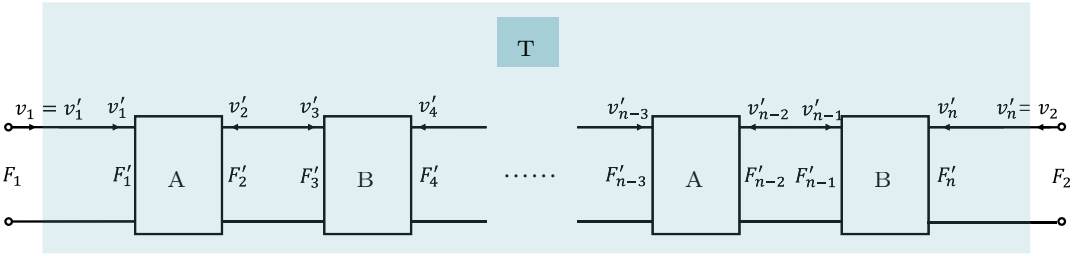


Fig. 4. Two-terminal networks.

According to Eq. (21), the relationship between the vibration velocity ratio and frequency, i.e., the frequency response function, can be obtained. The mathematical software Wolfram Mathematica 11.3 is used to calculate the frequency response function. The material used is titanium beta-21s and the material parameters are shown in Table 1.

Table 1. Material parameters of used materials.

Parameters	Value		
	PZT-4		
ρ (kg/m^3)	7500		
c_{11}^{E} (10^{10} N/m^2)	13.9		
c_{12}^{E} (10^{10} N/m^2)	7.78		
c_{13}^{E} (10^{10} N/m^2)	7.43		
c_{33}^{E} (10^{10} N/m^2)	11.5		
e_{31} (N·m/V)	–5.2		
e_{33} (N·m/V)	15.1		
$\varepsilon_{33}^{\mathrm{s}}$ (10^{-9} C/m)	5.62		
Parameters	Value		
	Aluminum 6083-T83	Titanium beta-21s	Steel AISI 4340
ρ (kg/m^3)	2700	4940	7850
E (10^9 N/m^2)	69	105	205
σ	0.33	0.33	0.28

The electromechanical equivalent circuit of the ultrasonic scalpel is shown in Fig. 5(a). The electrodes are thin which can be neglected in the analysis.

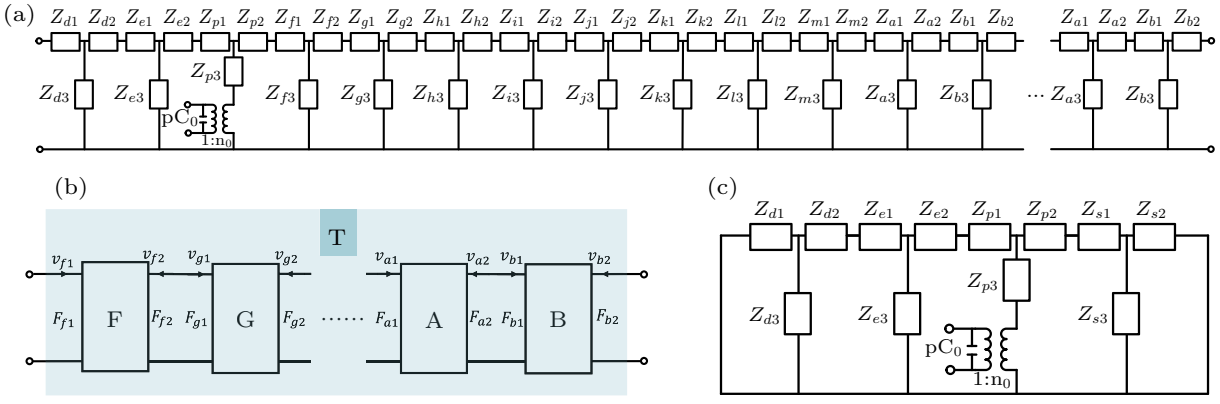


Fig. 5. Theoretical analysis of ultrasonic scalpel. (a) Electromechanical equivalent circuit of ultrasonic scalpel. (b) Two-terminal network. (c) Simplified electromechanical equivalent circuit.

The expressions of Z_{d1}, Z_{d2}, Z_{d3}, Z_{e1}, Z_{e2}, Z_{e3}, Z_{p1}, Z_{p2}, Z_{p3}, Z_{f1}, Z_{f2}, Z_{f3}, Z_{g1}, Z_{g2}, Z_{g3}, Z_{h1}, Z_{h2}, Z_{h3}, Z_{i1}, Z_{i2}, Z_{i3}, Z_{j1}, Z_{j2}, Z_{j3}, Z_{k1}, Z_{k2}, Z_{k3}, Z_{l1}, Z_{l2}, Z_{l3}, Z_{m1}, Z_{m2}, Z_{m3} are shown in Table 2. p is the number of piezoelectric ceramics,

$$C_0 = \frac{p\varepsilon_{33}^{\mathrm{T}}\left(1-K_{33}^2\right)S_p}{l_p}, \quad n_0 = \frac{d_{33}S_p}{s_{33}^{\mathrm{E}}l_p},$$

where $\varepsilon_{33}^{\mathrm{T}}$, K_{33}, d_{33}, and s_{33}^{E} are the dielectric constant, electromechanical coupled coefficient, the piezoelectric constant, and the elastic compliance of piezoelectric ceramics.

Table 2. Expression of impedance.

	Z_1	Z_2	Z_3
D	$Z_{d1}=\mathrm{j}\rho_{\mathrm{g}}c_{\mathrm{g}}S_d\tan\left(\frac{k_{\mathrm{g}}l_d}{2}\right)$	$Z_{d2}=\mathrm{j}\rho_{\mathrm{g}}c_{\mathrm{g}}S_d\tan\left(\frac{k_{\mathrm{g}}l_d}{2}\right)$	$Z_{d3}=\frac{\rho_{\mathrm{g}}c_{\mathrm{g}}S_d}{\mathrm{j}\sin(k_{\mathrm{g}}l_d)}$
E	$Z_{e1}=\mathrm{j}\rho_{\mathrm{g}}c_{\mathrm{g}}S_e\tan\left(\frac{k_{\mathrm{g}}l_e}{2}\right)$	$Z_{e2}=\mathrm{j}\rho_{\mathrm{g}}c_{\mathrm{g}}S_e\tan\left(\frac{k_{\mathrm{g}}l_e}{2}\right)$	$Z_{e3}=\frac{\rho_{\mathrm{g}}c_{\mathrm{g}}S_e}{\mathrm{j}\sin(k_{\mathrm{g}}l_e)}$
P	$Z_{p1}=\mathrm{j}\rho_{\mathrm{p}}c_{\mathrm{p}}S_p\tan\left(\frac{pk_pl_p}{2}\right)$	$Z_{p2}=\mathrm{j}\rho_{\mathrm{p}}c_{\mathrm{p}}S_p\tan\left(\frac{pk_pl_p}{2}\right)$	$Z_{p3}=\frac{\rho_{\mathrm{p}}c_{\mathrm{p}}S_p}{\mathrm{j}\sin(pk_pl_p)}$
F	$Z_{f1}=\mathrm{j}\rho_{\mathrm{l}}c_{\mathrm{l}}S_f\tan\left(\frac{k_{\mathrm{l}}l_f}{2}\right)$	$Z_{f2}=\mathrm{j}\rho_{\mathrm{l}}c_{\mathrm{l}}S_f\tan\left(\frac{k_{\mathrm{l}}l_f}{2}\right)$	$Z_{f3}=\frac{\rho_{\mathrm{l}}c_{\mathrm{l}}S_f}{\mathrm{j}\sin(k_{\mathrm{l}}l_f)}$
G	$Z_{g1}=-\mathrm{j}\frac{\rho_{\mathrm{l}}c_{\mathrm{l}}S_{\mathrm{g1}}}{k_{\mathrm{l}}l_{\mathrm{g}}}\left(\sqrt{\frac{S_{\mathrm{g2}}}{S_{\mathrm{g1}}}}-1\right)$ $-\mathrm{j}\rho_{\mathrm{l}}c_{\mathrm{l}}S_{\mathrm{g1}}\cot\left(k_{\mathrm{l}}l_{\mathrm{g}}\right)+\mathrm{j}\frac{\rho_{\mathrm{l}}c_{\mathrm{l}}\sqrt{S_{\mathrm{g1}}S_{\mathrm{g2}}}}{\sin(k_{\mathrm{l}}l_{\mathrm{g}})}$	$Z_{g2}=-\mathrm{j}\frac{\rho_{\mathrm{l}}c_{\mathrm{l}}S_{\mathrm{g2}}}{k_{\mathrm{l}}l_{\mathrm{g}}}\left(\sqrt{\frac{S_{\mathrm{g1}}}{S_{\mathrm{g2}}}}-1\right)$ $-\mathrm{j}\rho_{\mathrm{l}}c_{\mathrm{l}}S_{\mathrm{g2}}\cot\left(k_{\mathrm{l}}l_{\mathrm{g}}\right)+\mathrm{j}\frac{\rho_{\mathrm{l}}c_{\mathrm{l}}\sqrt{S_{\mathrm{g1}}S_{\mathrm{g2}}}}{\sin\left(k_{\mathrm{l}}l_{\mathrm{g}}\right)}$	$Z_{g3}=\frac{\rho_{\mathrm{l}}c_{\mathrm{l}}\sqrt{S_{\mathrm{g1}}S_{\mathrm{g2}}}}{\mathrm{j}\sin(k_{\mathrm{l}}l_{\mathrm{g}})}$
H	$Z_{h1}=\mathrm{j}\rho_{\mathrm{l}}c_{\mathrm{l}}S_h\tan\left(\frac{k_{\mathrm{l}}l_h}{2}\right)$	$Z_{h2}=\mathrm{j}\rho_{\mathrm{l}}c_{\mathrm{l}}S_h\tan\left(\frac{k_{\mathrm{l}}l_h}{2}\right)$	$Z_{h3}=\frac{\rho_{\mathrm{l}}c_{\mathrm{l}}S_h}{\mathrm{j}\sin(k_{\mathrm{l}}l_h)}$
I	$Z_{i1}=\mathrm{j}\rho_{\mathrm{l}}c_{\mathrm{l}}S_i\tan\left(\frac{k_{\mathrm{l}}l_i}{2}\right)$	$Z_{i2}=\mathrm{j}\rho_{\mathrm{l}}c_{\mathrm{l}}S_i\tan\left(\frac{k_{\mathrm{l}}l_i}{2}\right)$	$Z_{i3}=\frac{\rho_{\mathrm{l}}c_{\mathrm{l}}S_i}{\mathrm{j}\sin(k_{\mathrm{l}}l_i)}$
J	$Z_{j1}=\mathrm{j}\rho_{\mathrm{l}}c_{\mathrm{l}}S_j\tan\left(\frac{k_{\mathrm{l}}l_j}{2}\right)$	$Z_{j2}=\mathrm{j}\rho_{\mathrm{l}}c_{\mathrm{l}}S_j\tan\left(\frac{k_{\mathrm{l}}l_j}{2}\right)$	$Z_{j3}=\frac{\rho_{\mathrm{l}}c_{\mathrm{l}}S_i}{\mathrm{j}\sin(k_{\mathrm{l}}l_i)}$
K	$Z_{k1}=-\mathrm{j}\frac{\rho_{\mathrm{l}}c_{\mathrm{l}}S_{k1}}{k_{\mathrm{l}}l_k}\left(\sqrt{\frac{S_{k2}}{S_{k1}}}-1\right)$ $-\mathrm{j}\rho_{\mathrm{l}}c_{\mathrm{l}}S_{k1}\cot\left(k_{\mathrm{l}}l_k\right)+\mathrm{j}\frac{\rho_{\mathrm{l}}c_{\mathrm{l}}\sqrt{S_{k1}S_{k2}}}{\sin(k_{\mathrm{l}}l_k)}$	$Z_{k1}=-\mathrm{j}\frac{\rho_{\mathrm{l}}c_{\mathrm{l}}S_{k2}}{k_{\mathrm{l}}l_k}\left(\sqrt{\frac{S_{k1}}{S_{k2}}}-1\right)$ $-\mathrm{j}\rho_{\mathrm{l}}c_{\mathrm{l}}S_{k2}\cot\left(k_{\mathrm{l}}l_k\right)+\mathrm{j}\frac{\rho_{\mathrm{l}}c_{\mathrm{l}}\sqrt{S_{k1}S_{k2}}}{\sin(k_{\mathrm{l}}l_k)}$	$Z_{k3}=\frac{\rho_{\mathrm{l}}c_{\mathrm{l}}\sqrt{S_{k1}S_{k2}}}{\mathrm{j}\sin(k_{\mathrm{l}}l_k)}$
L	$Z_{l1}=\mathrm{j}\rho_{\mathrm{l}}c_{\mathrm{l}}S_{\mathrm{l}}\tan\left(\frac{k_{\mathrm{l}}l_{\mathrm{l}}}{2}\right)$	$Z_{l2}=\mathrm{j}\rho_{\mathrm{l}}c_{\mathrm{l}}S_{\mathrm{l}}\tan\left(\frac{k_{\mathrm{l}}l_{\mathrm{l}}}{2}\right)$	$Z_{l3}=\frac{\rho_{\mathrm{l}}c_{\mathrm{l}}S_{\mathrm{l}}}{\mathrm{j}\sin(k_{\mathrm{l}}l_{\mathrm{l}})}$
M	$Z_{m1}=\mathrm{j}\rho_{\mathrm{t}}c_{\mathrm{t}}S_m\tan\left(\frac{k_{\mathrm{t}}l_m}{2}\right)$	$Z_{m2}=\mathrm{j}\rho_{\mathrm{t}}c_{\mathrm{t}}S_m\tan\left(\frac{k_{\mathrm{t}}l_m}{2}\right)$	$Z_{m3}=\frac{\rho_{\mathrm{t}}c_{\mathrm{t}}S_m}{\mathrm{j}\sin(k_{\mathrm{t}}l_m)}$

In Table 2, ρ_{g}, ρ_{l}, ρ_{t}, and ρ_{p} are the density for steel AISI 4340, aluminum 6083-T83, titanium beta-21s, and PZT-4, $k_{\mathrm{g}}=\omega/c_{\mathrm{g}}$, $k_{\mathrm{l}}=\omega/c_{\mathrm{l}}$, $k_{\mathrm{p}}=\omega/c_{\mathrm{p}}$, $k_{\mathrm{t}}=\omega/c_{\mathrm{t}}$, $c_{\mathrm{g}}=\sqrt{E_{\mathrm{g}}/\rho_{\mathrm{g}}}$, $c_{\mathrm{l}}=\sqrt{E_{\mathrm{l}}/\rho_{\mathrm{l}}}$, $c_{\mathrm{p}}=\sqrt{1/(s_{33}^{\mathrm{E}}\rho_{\mathrm{p}})}$, $c_{\mathrm{t}}=\sqrt{E_{\mathrm{t}}/\rho_{\mathrm{t}}}$, E_{g}, E_{l}, E_{t} are the Young's modulus of steel AISI 4340, aluminum 6083-T83, titanium beta-21s.

Here, the electromechanical equivalent circuit of F, G, H, I, J, K, L, M, A, and B can be regarded as a two-port network, as shown in Fig. 5(b). Since each two-port network is a cascade relationship, the relationship between force and vibration velocity can be rewritten as follows:

$$\begin{bmatrix} F_{n1} \\ v_{n1} \end{bmatrix} = T_n \begin{bmatrix} F_{n2} \\ -v_{n2} \end{bmatrix}, \tag{22}$$

where

$$T_n = \begin{bmatrix} A_n & B_n \\ C_n & D_n \end{bmatrix}, \quad A_n = \frac{Z_{11n}}{Z_{21n}},$$
$$B_n = \frac{\Delta Z_n}{Z_{21n}}, \quad C_n = \frac{1}{Z_{21n}}, \quad D_n = \frac{Z_{22n}}{Z_{21n}},$$
$$Z_{11n} = Z_{n1} + Z_{n3}, \quad Z_{22n} = Z_{n2} + Z_{n3},$$
$$Z_{12n} = Z_{21n} = Z_{n3}, \quad \Delta Z_n = \begin{vmatrix} Z_{11n} & Z_{12n} \\ Z_{21n} & Z_{22n} \end{vmatrix}.$$
$$n = f,g,h,i,j,k,l,m,a,b.$$

According to the two-port cascading, the following expression can be obtained:

$$T_{\mathrm{t}} = \begin{bmatrix} A_{\mathrm{t}} & B_{\mathrm{t}} \\ C_{\mathrm{t}} & D_{\mathrm{t}} \end{bmatrix} = T_f T_{\mathrm{g}} T_h T_i T_j T_k T_{\mathrm{l}} T_m T. \tag{23}$$

When the ultrasonic scalpel vibrates freely, it can be regarded as no load. Figure 5(c) shows the simplified electromechanical equivalent circuit, where $Z_{s1}=A_{\mathrm{t}}/C_{\mathrm{t}}-\Delta T_{\mathrm{t}}/C_{\mathrm{t}}$, $Z_{s2}=\Delta T_{\mathrm{t}}/C_{\mathrm{t}}$, $Z_{s3}=D_{\mathrm{t}}/C_{\mathrm{t}}-\Delta T_{\mathrm{t}}/C_{\mathrm{t}}$, $\Delta T_{\mathrm{t}}=\begin{vmatrix} A_{\mathrm{t}} & B_{\mathrm{t}} \\ C_{\mathrm{t}} & D_{\mathrm{t}} \end{vmatrix}$. The input impedance of the ultrasonic scalpel is

$$Z_{\mathrm{eq}} = \frac{Z_{\mathrm{mi}}}{n_0^2 + \mathrm{j}\omega C_0 Z_{\mathrm{mi}}}. \tag{24}$$

The admittance is the reciprocal of the input impedance, which can be expressed as

$$Y = \frac{1}{Z_{\mathrm{eq}}} = \frac{n_0^2 + \mathrm{j}\omega C_0}{Z_{\mathrm{mi}}}, \tag{25}$$

where $Z_{\mathrm{mi}} = Z_{p3} + Z_v Z_\omega/(Z_v + Z_\omega)$, $Z_v = Z_{p2} + Z_{s1} + Z_{s2}Z_{s3}/(Z_{s2}+Z_{s3})$, $Z_w = Z_{p1} + Z_{e2} + Z_q Z_{e3}/(Z_q + Z_{e3})$, $Z_q = Z_{e1} + Z_{d2} + Z_{d1}Z_{d3}/(Z_{d1}+Z_{d3})$. According Eqs. (24) and (25), the frequency response curves of impedance and admittance can be obtained by using the mathematical software Wolfram Mathematica 11.3. The geometric dimensions of the ultrasonic scalpel are $S_d = 96\sqrt{3}$ mm^2, $S_e = 8^2\pi$ mm^2, $S_p =$

$8^2\pi$ mm^2, $S_f = 8^2\pi$ mm^2, $S_{g1} = 8^2\pi$ mm^2, $S_{g2} = 5.7^2\pi$ mm^2, $S_h = 5.7^2\pi$ mm^2, $S_i = 5.95^2\pi$ mm^2, $S_j = 9.45^2\pi$ mm^2, $S_k = 5.27^2\pi$ mm^2, $S_l = 3.19^2\pi$ mm^2, $S_m = 2^2\pi$ mm^2, $l_d = 4.5$ mm, $l_e = 4.5$ mm, $l_p = 2.5$ mm, $l_f = 2.5$ mm, $l_g = 4.37$ mm, $l_h = 15.77$ mm, $l_i = 22.23$ mm, $l_j = 2.6$ mm, $l_k = 6.66$ mm, $l_l = 19.24$ mm, and $l_m = 405 - 7a$ mm. For the ultrasonic scalpel of non-PnCs structures, $a = 0$. Therefore, $l_m = 405$ mm.

2.3. FEM

The FEM has been widely used in the analysis of PnCs. Therefore, the commercial software COMSOL Multiphysics is used to analyze the frequency response function of the blade. An acceleration response of magnitude 1 m/s^2 is applied to one end of the blade, and a probe is added to the other end, as shown in Fig. 6. By processing the data of the probe, the frequency response function of the blade can be obtained. The geometrical dimensions and material parameters used are the same as those in the electromechanical equivalent circuit method.

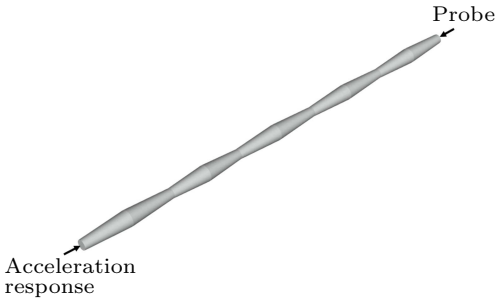


Fig. 6. Calculation method of frequency response function for FEM.

For the analysis of the vibration characteristics of ultrasonic scalpel, the piezoelectric device module is used. The geometric model as shown in Fig. 1 is established in the finite element software, where the dimensions and material parameters used are consistent with those of the electromechanical equivalent circuit method. Free boundaries are selected, and the applied voltage is 1 V. In addition, the displacement distribution on this intercept line at the resonance frequency can be obtained by defining an intercept line in the length direction of the ultrasonic scalpel.

3. Results and discussion

3.1. Verification of theoretical validity

In Ref. [24], a vibration experiment of one-dimensional PnCs was studied. A unit cell included an aluminum rod and a PMMA rod, as shown in Fig. 7(a). The diameter and length of each aluminum rod and PMMA rod were 10 mm and 75 mm. Vibration excitation is applied to one end, and the output amplitude of acceleration is measured at the other end. In order to verify the validity of the electromechanical equivalent circuit method, the results obtained by the electromechanical equivalent circuit method are compared with the experimental results in Ref. [24]. According to the boundary conditions at the contacting surfaces, the electromechanical equivalent circuits of the metal cylinder and the PMMA cylinder can be cascaded, as shown in Fig. 7(b). The impedance expressions in Fig. 7(b) are

$$
\begin{aligned}
Z_{al1} &= Z_{al2} = \mathrm{j}\rho_{al}c_{al}S_{al}\tan(k_{al}l_{al}/2),\\
Z_{al3} &= \frac{\rho_{al}c_{al}S_{al}}{\mathrm{j}\sin(k_{al}l_{al})},\\
Z_{pm1} &= Z_{pm2} = \mathrm{j}\rho_{pm}c_{pm}S_{pm}\tan(k_{pm}l_{pm}/2),\\
Z_{pm3} &= \frac{\rho_{pm}c_{pm}S_{pm}}{\mathrm{j}\sin(k_{pm}l_{pm})},
\end{aligned}
$$

where $k_{al} = \omega/c_{al}$, $c_{al} = \sqrt{E_{al}/\rho_{al}}$, ρ_{al}, E_{al}, S_{al}, and l_{al} are the bulk density, Young's modulus, cross-sectional area and length of aluminum rod, respectively. $k_{pm} = \omega/c_{pm}$, $c_{pm} = \sqrt{E_{pm}/\rho_{pm}}$, ρ_{pm}, E_{pm}, S_{pm}, and l_{pm} are the bulk density, Young's modulus, cross-sectional area and length of PMMA rod, respectively.

Figure 8 illustrates comparison between the frequency response function of the electromechanical equivalent circuit method and experiment, where figure 8(a) is the experimental results in Ref. [24], and figure 8(b) is the results by the electromechanical equivalent circuit method. The band gaps for experimental results in Ref. [24] are 5.4 kHz–13.6 kHz and 15.9 kHz–24.8 kHz, and the band gaps calculated by the electromechanical equivalent circuit method are 4.8 kHz–11.6 kHz and 14.3 kHz–23.5 kHz. The material parameters used for aluminum are consistent with those in Table 1. For PMMA, $\rho_{pm} = 1180$ kg/m^3, $E_{pm} = 4.35$ GPa. The results obtained by the equivalent circuit method are close to the experimental results in Ref. [24]. Since the material parameters are not given in Ref. [24], the error is mainly caused by the different material parameters.

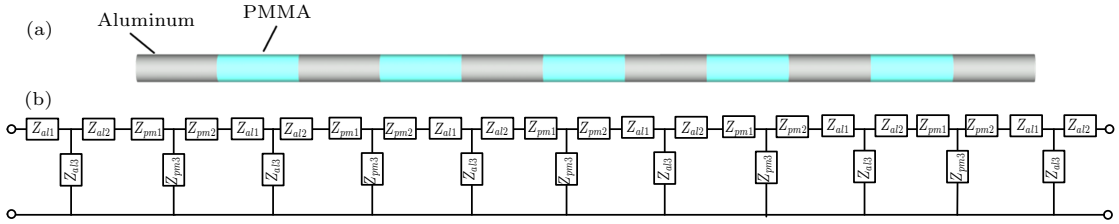


Fig. 7. Validation of electromechanical equivalent circuit method: (a) PnCs structure in Ref. [24], (b) the electromechanical equivalent circuit for PnCs structure.

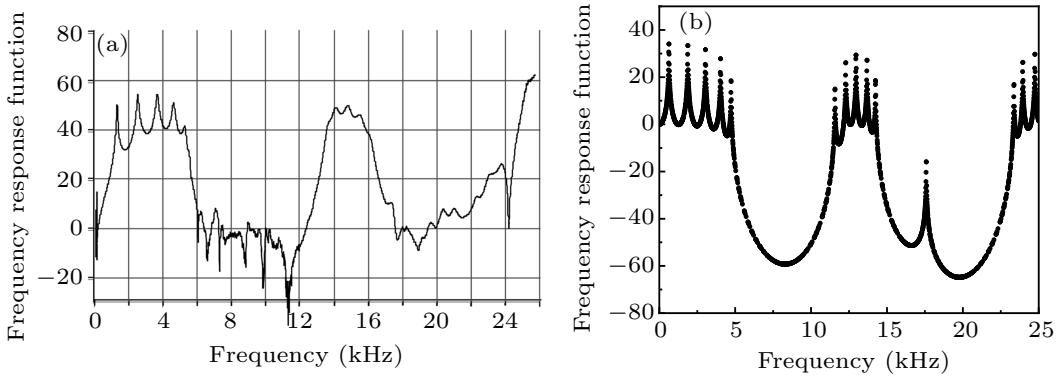


Fig. 8. Comparisons between the frequency response function of the electromechanical equivalent circuit method and experiment: (a) experimental results in Ref. [24], (b) results of the electromechanical equivalent circuit method.

3.2. Frequency response function

Exploring the bandgap law of the fusiform PnCs structure is instrumental for subsequent device design. Here, the frequency response functions of the three structures are analyzed by the electromechanical equivalent circuit method and the FEM for the cone, exponent, and catenary, respectively, as shown in Fig. 9. The dimensions of the blade used in the calculation are as follows: $d_1 = 2.5$ mm, $d_2 = 4$ mm, $a_1 = a_2 = 27$ mm. The number of periods is 7. It is shown that Bragg band gap is existed for blades based on fusiform PnCs. The band gap width for the cone, exponent, and catenary are 35.0 kHz–51.0 kHz, 35 kHz–51.1 kHz, and 34.7 kHz–51.2 kHz, respectively. The area function has a minor effect on the width of the bandgap, with the widest bandgap range for the cone. In addition, a second band gap appears in the 82.7 kHz–89.9 kHz range for the blade of the catenary structure. The results of electromechanical equivalent circuits are in good agreement with those of FEM, which shows the validity of the electromechanical equivalent circuit method in calculating the vibration transmission characteristics curve.

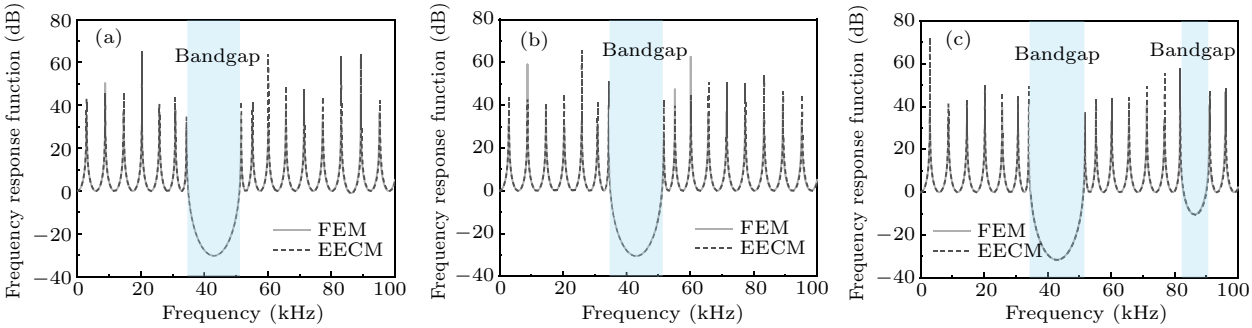


Fig. 9. Frequency response function for the blade of (a) cone, (b) exponent, (c) catenary.

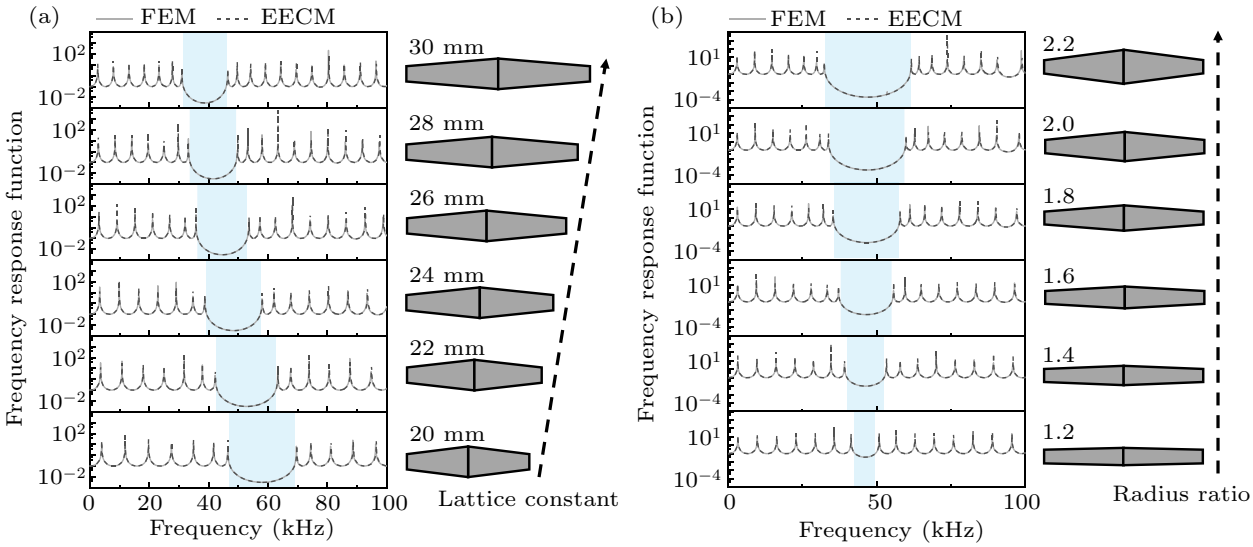


Fig. 10. Frequency response function as a function of (a) lattice constant and (b) radius ratio for one-dimensional fusiform PnCs structure.

The frequency response function is calculated with the lattice constants and radius ratios of the one-dimensional fusiform PnCs structure, as shown in Fig. 10, where the blue part is the vibrational bandgap, and the area function adopted is conical. In the case of $d_1 = 2.5$ mm, $d_2 = 4$ mm, periods $= 7$, the bandwidth for the vibration bandgap decreases and shifts towards lower frequencies with the lattice constants of the one-dimensional fusiform PnCs structure from 20 mm to 30 mm, as shown in Fig. 10(a). Because the band gap type of fusiform PnCs structure is Bragg band gap, the center frequency of the first band gap is generally located near $c/(2a)$ (c is the speed of sound), so as the lattice constant increases, the center frequency shifts to the low frequency. In the case of $a = 25$ mm, periods $= 7$, the bandwidth for the vibration bandgap gradually increases as the radius ratio (d_2/d_1) of the one-dimensional fusiform PnCs structure goes from 1.2 to 2.2, as shown in Fig. 10(b). As the radius ratio increases, a greater impedance mismatch is induced, which is beneficial for bandgap performance, therefore the bandwidth of the bandgap becomes wider. In addition, the stiffness of the structure increases with the increase of the radius ratio, so the center frequency of the band gap increases with the increase of the radius ratio.

The vibration of the blade in the band gap range will be suppressed, so the working frequency cannot be designed in the band gap range. The band gap should be designed near the working frequency, which can well suppress other vibration modes near the working frequency. Thus, the interference to the working frequency can be reduced.

3.3. Analysis of vibration characteristics for ultrasonic scalpel

It is expected to suppress other resonance modes by designing the working frequency of the ultrasonic scalpel near the vibration band gap. The analysis for the frequency response curves of admittance for the ultrasonic scalpel is necessary. The area functions have a relatively small effect on the band gap width. Considering the difficulty of manufacturing, the vibration characteristics of the conical structure are analyzed.

Figure 11 shows the frequency response curves of admittance, where the dimensions of the transducer and horn are the same as mentioned in Section 2, the dimensions of the blade are as follows: $d_1 = 2.5$ mm, $d_2 = 4$ mm, $a_1 = a_2 = 27$ mm, periods $= 7$. The results of theoretical model are in good agreement with those of the FEM. Combined with the vibration mode analysis, the working frequency of the ultrasonic scalpel can be determined. There are unnecessary vibration modes around the working frequency of the ultrasonic scalpel, as shown in Fig. 11(a). For ultrasonic scalpel based on PnCs, other vibration modes near working frequency are isolated, as shown in Fig. 11(b). It illustrates that the PnCs structure can effectively suppress other modes near the working frequency for the ultrasonic scalpel. For more practical designs, the PnC structure can still achieve this effect after the introduction of curved head in the ultrasonic scalpel (more details shown in Section S1 of supporting information).

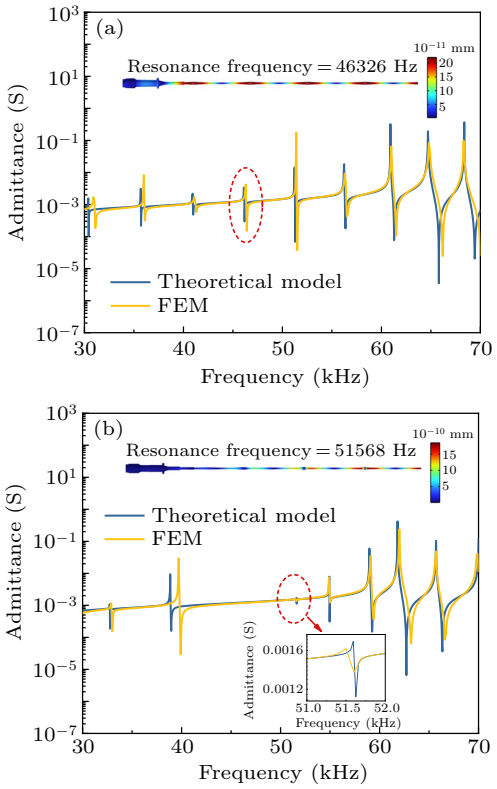


Fig. 11. The frequency response curves of admittance: (a) conventional ultrasonic scalpel, (b) ultrasonic scalpel based on fusiform PnCs.

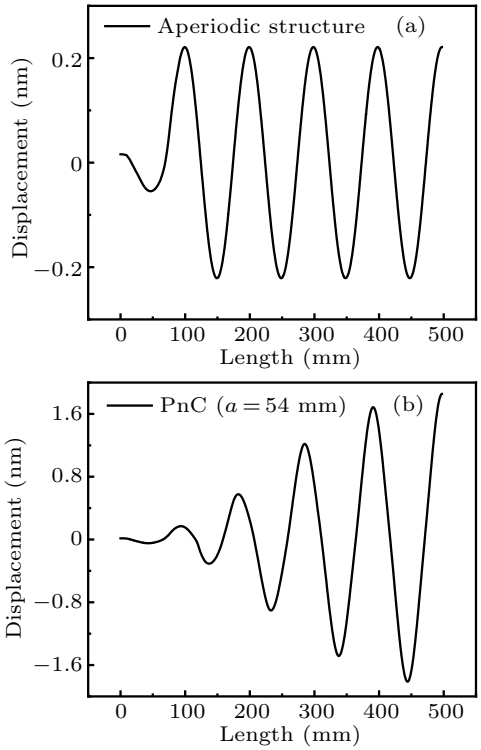


Fig. 12. Displacement distribution for (a) conventional ultrasonic scalpel and (b) ultrasonic scalpel based on PnCs.

In addition, figure 12 shows the vibration displacement distribution of the conventional ultrasonic scalpel as well as the ultrasonic scalpel based on the PnCs. It can be seen that the vibration displacement for the ultrasonic scalpel based on PnCs is larger than that for the conventional ultrasonic scalpel. Therefore, the fusiform PnCs structure have the effect of amplifying the displacement, which is similar to the function of the ultrasonic horn. The truncation resonance is that the elastic wave increases exponentially from the excitation point and shows high amplitude at the boundary.[25] This phenomenon is a notable similarity to the vibration amplitude pattern observed in the ultrasonic scalpel based on PnC structures. Consequently, there may exist a potential correlation between the enhanced amplitude observed in ultrasonic scalpel based on PnCs and the truncation resonance.

4. Conclusion and perspectives

The ultrasonic scalpel based on the PnCs is designed to suppress the unnecessary vibration modes that lead to a decrease of the ultrasonic scalpel efficiency. A practical and accurate theoretical model is proposed, aiming to effectively evaluate the frequency response functions for the blades and the frequency response curves of admittance for ultrasonic scalpel. Bragg band gaps exist in fusiform PnCs, and the area function, lattice constant, and radius ratio affect the band gap range. The fusiform PnCs can effectively inhibit other vibration modes near the working frequency of the ultrasonic scalpel. In addition, the fusiform PnCs have the effect of amplifying the displacement of the ultrasonic scalpel, which is similar to the function of a horn.

Acknowledgements

Project supported by the National Natural Science Foundation of China (Grant Nos. 62204112, 12174240, and 11874253) and the Natural Science Foundation of Jiangsu Province, China (Grant No. BK20220774).

References

[1] Sawaizumi M, Maruyama Y, Onishi K, Iwahira Y and Okada E 1996 *Ann. Plas. Surg.* **36** 124
[2] Zhang S B, Chen Z R, Wu H Q, Li G Z and Wu Y B 2023 *Ultrasonics* **131** 106966
[3] Lee T, Luo W, Li Q C, Demirci H and Guo L J 2017 *Small* **13** 1701555
[4] Schafer M E 2023 *IEEE T. Ultrason. Ferr.* **70** 147
[5] Moon R D C, Srikandarajah N, Clark S, Wilby M J and Pigott T D 2020 *Brit. J. Neurosurg* **35** 775
[6] Lee S H, Nguyen T K, Ong W S, Haaland B, Tay G C A, Tan N C, Tan H K, Ng J C F and Iyer N G 2019 *Ann. Surg. Oncol.* **26** 4414
[7] Bozkurt G, Turri-Zanoni M, Russo F, Elhassan H A, Castelnuovo P, Castelnuovo P and Battaglia P 2019 *World Neurosurgery* **123** 23
[8] Chen X L, Chen X Z, Lu Z H, Wang L, Yang K, Hu J K, Zhang B, Chen Z X, Chen J P and Zhou Z G 2014 *Plos One* **9** e103330
[9] Sun S, Zhang Q, Zhao C S and Cai J 2014 *Oncol. Lett.* **8** 145
[10] Li J H, Dong X Y, Zhang G H, Guo Z C, Zhang G K and Shi C Y 2021 *IEEE Access* **9** 10951
[11] Ying C, Zhou Z Y and Zhang G H 2005 *Ultrasound Med. Biol.* **32** 415
[12] Kushwaha M S, Halevi P, Dobrzynski L and Djafari-Rouhani B 1993 *Phys. Rev. Lett.* **71** 2022
[13] Vasseur J O, Deymier P A, Chenni B, Djafari-Rouhani B, Dobrzynski L and Prevost D 2001 *Phys. Rev. Lett.* **86** 3012
[14] Wang Y F, Wang Y Z, Wu B, Chen W Q and Wang Y S 2020 *Appl. Mech. Rev.* **72** 040801
[15] Lu M H, Feng L and Chen Y F 2009 *Mater. Today* **12** 34
[16] Wang C M, Xiao W Q, Wu D H, Wang S, Lin C M, Luo Y Y, Xiao J J, Yao K H and Xu Z H 2020 *Appl. Acoust.* **166** 107352
[17] Zhang Q C, Lee D H, Zheng L, Ma X J, Meyer S I, He L, Ye H, Gong Z, Zhen B, Lai K J and Johnson A T C 2022 *Nat. Electron.* **5** 157
[18] Zhao W, Song T, Tian M, Xu G G, Gao X L and Sun X W 2021 *Appl. Phys. A-Mater.* **127** 490
[19] Wang S and Lin S Y 2019 *Ultrasonics* **99** 105954
[20] Zhang Y F, Yu D L and Wen J H 2017 *Extreme Mech. Lett.* **12** 2
[21] Ruan Y D, Liang X, Hua X Y, Zhang C, Xia H and Li C 2021 *Ocean Eng.* **225** 108804
[22] Vasileiadis T, Varghese J, Babacic V, Gomis-Bresco J, Urrios D N and Graczykowski B 2021 *J. Appl. Phys.* **129** 160901
[23] Lu Q F, Liu C C and Wang P 2022 *Compos. Struct.* **292** 115650
[24] Jensen J S, Sigmund O, Thomsen J J and Bendsøe M P 2002 15*th Nordic Seminar on Computational Mechanics*, October 18–19 (Aalborg, Denmark) pp. 63–66
[25] Park S, Yan, R F and Matlack K H 2024 *J. Acoust. Soc. Am.* **155** 791